Asteroid (3200) Phaethon: Colors, Phase Curve, Limits on Cometary Activity, and Fragmentation

Maryam Tabeshian[1] , Paul Wiegert[1,2] , Quanzhi Ye[3,4] , Man-To Hui[5] , Xing Gao[6], and Hanjie Tan[7]

[1] Department of Physics and Astronomy, The University of Western Ontario, London, ON N6A 3K7, Canada; mtabeshi@uwo.ca
[2] Centre for Planetary Science and Exploration, The University of Western Ontario, London, ON N6A 3K7, Canada
[3] Division of Physics, Mathematics and Astronomy, California Institute of Technology, Pasadena, CA, 91125, USA
[4] Infrared Processing and Analysis Center, California Institute of Technology, Pasadena, CA, 91125, USA
[5] Department of Earth, Planetary and Space Sciences, UCLA, Los Angeles, CA, 90095, USA
[6] Xinjiang Astronomical Observatory, Urumqi, Xinjiang 830011, People's Republic of China
[7] Department of Physics, National Central University, 32001, Taiwan

Abstract

We report on a multiobservatory campaign to examine asteroid 3200 Phaethon during its 2017 December close approach to Earth, in order to improve our measurements of its fundamental parameters, and to search for surface variations, cometary activity, and fragmentation. The mean colors of Phaethon are $B - V = 0.702 \pm 0.004$, $V - R = 0.309 \pm 0.003$, and $R - I = 0.266 \pm 0.004$, neutral to slightly blue, consistent with previous classifications of Phaethon as a F-type or B-type asteroid. Variations in Phaethon's $B - V$ colors (but not $V - R$ or $R - I$) with observer sublatitude are seen and may be associated with craters observed by the Arecibo radar. High-cadence photometry over phases from $20°$ to $100°$ allows a fit to the values of the HG photometric parameters; $H = 14.57 \pm 0.02$, 13.63 ± 0.02, 13.28 ± 0.02, 13.07 ± 0.02; $G = 0.00 \pm 0.01$, -0.09 ± 0.01, -0.10 ± 0.01, -0.08 ± 0.01 in the *BVRI* filters respectively; the negative G values are consistent with other observations of F-type asteroids. Light-curve variations were seen that are also consistent with concavities reported by Arecibo, indicative of large craters on Phaethon's surface whose ejecta may be the source of the Geminid meteoroid stream. A search for gas/dust production sets an upper limit of $0.06 \pm 0.02 \, \mathrm{kg \, s^{-1}}$ when Phaethon was 1.449 au from the Sun, and $0.2 \pm 0.1 \, \mathrm{kg \, s^{-1}}$ at 1.067 au. A search for meter-class fragments accompanying Phaethon did not find any whose on-sky motion was not also consistent with background main-belt asteroids.

Key words: comets: general – minor planets, asteroids: general – minor planets, asteroids: individual (3200 Phaethon)

Supporting material: animation

1. Introduction

Although dynamically associated with the Geminid meteoroid stream (Whipple 1983), the absence of cometary activity or mass loss from the near-Earth asteroid (3200) Phaethon since its discovery has made it the target for numerous studies. Given the short dynamical lifetime of Geminid meteoroids ($\sim 10^3$ yr; Ryabova 2007), astronomers speculated that Phaethon must have undergone some recent cometary activity that may have continued to the present time. This idea was further strengthened when NASA-*STEREO* coronal imaging observations of Phaethon in 2009 by Jewitt & Li (2010) and three years later by Li & Jewitt (2013) showed anomalous and sudden brightening of the asteroid at perihelion ($q = 0.14$ au) by a factor of 2, which was attributed to the release of solid grains from the nucleus. Further observations using the NASA-*STEREO* coronal imaging spacecraft by Jewitt et al. (2013) confirmed that Phaethon had a comet-like dust tail when it was just past perihelion in both 2009 and 2012; Hui & Li (2017) analyzed Phaethon around its 2016 perihelion and observed similar behavior. However, whether Phaethon is an asteroid or an extinct cometary nucleus is still a matter of debate.

While Davies (1986) had suggested that Phaethon is an extinct comet, Jewitt & Li (2010) argued the dust grains were likely released through desiccation cracking of the surface and thermal fracture due to extensive heating (~ 1000 K) near perihelion rather than volatile sublimation. From the properties and morphology of the tail, the effective radius of the dust particles and their combined mass were estimated to be $\sim 1 \, \mu$m and 3×10^5 kg, respectively, too low to explain the current Geminid meteoroid stream. On the other hand, using a 3D model of gas and heat transport in porous subsurface layers of Phaethon's interior, Boice et al. (2013) found that relatively pristine volatiles in the interior of Phaethon might still exist despite many perihelion passages over its short (1.49 yr) orbital period. Thus high-temperature processes as well as cometary outgassing may both be at work and the exact mechanism or mechanisms by which the Geminid meteoroid stream was produced remain unclear.

Even close to perihelion where Phaethon shows a dust tail, not only does it produce 100–1000 times less mass than needed, individual dust particles that are ejected from Phaethon are much smaller and less massive than typical meteoroids in the Geminid stream and are quickly removed by solar radiation pressure (Jewitt & Li 2010). Several alternative mechanisms have been proposed to explain how Phaethon could supply the Geminid stream mass. For instance, according to Jewitt et al. (2018), it is possible that the Geminids were produced as a result of a catastrophic event of unknown origin that occurred at some point within the past few thousand years. On the other hand, Yu et al. (2019) considered the possibility that Phaethon originated beyond the ice line—possibly having broken away from asteroid 2 Pallas as Phaethon's reflectance

spectra shows striking similarities to that of Pallas (see de León et al. 2010). Less than 1 Myr ago Phaethon would have moved to its present orbit, and so could have retained its subsurface ice until the present day.

Here we report ground-based observations of Phaethon by Gemini and the Canada–France–Hawaii Telescope (CFHT) on Maunakea, Hawaii as well the Xingming Observatory on Mt. Nanshan, Xinjiang, China obtained in 2017 November– December as the asteroid was approaching Earth. Our primary goals were to establish its colors and phase curve, to look for photometric variations across Phaethon's surface, to establish whether it has a coma and measure any mass loss during the observation period, and to search for meter-class fragments which might indicate a different mass-loss mechanism. We start in Section 2 by describing our observations, and then move to our analysis in Section 3. Finally, we present a summary and conclusions in Section 4.

2. Observations

Phaethon made its closest approach to Earth on 2017 December 16 when it came to 0.069 au of our planet. This was the closest Phaethon has been to Earth since its discovery in 1983 and provided an unprecedented opportunity to observe this apparent asteroid for possible cometary activity. Though outgassing will likely be highest when the asteroid is nearer perihelion, water ice-driven cometary activity can be expected at all distances less than about 3 au from the Sun (Delsemme & Miller 1971), and our sensitivity to such activity is much increased when we pass the asteroid closely. The previous closest approaches were 1984 December 21 at 0.24 au and 2007 December 10 at 0.12 au.[8]

Using multiple ground-based telescopes, we obtained data from Phaethon as it was approaching the Earth to provide a thorough examination of this interesting body. Nine nights of multicolor photometry with the 0.6 m telescope at the Xingming Observatory provide for high-cadence color information and a detailed phase curve. Gemini North and CFHT observations during this period allow an assessment of possible cometary activity and meter-scale fragmentation, and to determine Phaethon's current mass-loss rate, if any. The observations are summarized below.

2.1. CFHT

Observations were conducted using the MegaPrime/Mega-Cam wide-field imager at the 3.6 m CFHT. The charge-coupled device (CCD) detector is a mosaic of thirty-six 2112 × 4644 pixel chips, covering a total area of roughly $1 \times 1\,\mathrm{deg}^2$ on the sky at $0\rlap{.}''187$ per pixel (Boulade et al. 2003). The observations spanned 2017 November 15 12:30:22.74 UT– 13:24:43.16 UT during which we obtained eight 30 s exposure images, six of which were taken with Phaethon being tracked on the sky, the other two were tracked sidereally to allow stars in the field to provide stellar point-spread functions (PSFs) for comparison with Phaethon. These exposures were chosen to search for faint coma or other activity near the asteroid (see Section 3.1). We also obtained 4 images with a longer exposure time (900 s) which were used for searching for possible meter-sized fragments of Phaethon comoving with it in the volume of space around it (see Section 3.3). Because of the demands of

queue operations at the telescope, CFHT images were taken a few weeks before, and not at, Phaethon's closest approach. Phaethon's heliocentric and geocentric distances were $R = 1.449$ au and $\Delta = 0.611$ au during the time of observations.

2.2. Gemini

We obtained images of Phaethon during 2017 December 13 11:34:50.2 UT–12:33:04.2 UT using the Gemini Multi-Object Spectrograph on Gemini North (GMOS-N). The GMOS-N Hamamatsu array detector consists of three 2048 × 4176 chips of two different types arranged in a row. The images were obtained using the 12-amp mode. The Hamamatsu array detector has a resolution of $0\rlap{.}''0807$ per pixel. Twenty-four images with 2 s exposure times are analyzed here to search for coma (see Section 3.1), where in each case the asteroid was on the central chip (chip 6) near the center. Phaethon was tracked in all images except for 8, which were sidereally tracked to allow field stars to provide prototype PSFs. Phaethon's heliocentric and geocentric distances were $R = 1.067$ au and $\Delta = 0.094$ au during the time of observations.

2.3. Xingming Observatory

Observations were made using Ningbo bureau of Education and Xinjiang observatory Telescope (NEXT), a 60 cm reflector at Xingming Observatory in Mt. Nanshan, Xinjiang, China. The observatory coordinates are $43°28'15''$N and $87°10'39\rlap{.}''6$ E and it is at an elevation of 2080 m (IAU Code: C42). The FLI PL230 CCD camera used to obtain the data has a resolution of $0\rlap{.}''6$ per pixel. It has an array of 2048 × 2064 pixels, a field of view of 22 × 22 arcmin, and a focal length of 4800 mm. We used a total of 5245 light frames obtained between 2017 December 11 and 19 to measure the colors and phase curve (see Section 3.2). Phaethon's heliocentric and geocentric distances changed from $R = 1.109$ to 0.966 au and $\Delta = 0.133$ to 0.085 au during the time of observations as it approached the Earth. The frames were taken with Johnson *BVRI* filters and exposure times of 2, 3, or 6 s.

3. Results

3.1. Coma Search: CFHT and Gemini Data

If Phaethon exhibits no coma, its light profile should be that of a point source such as a star. If the asteroid does have detectable extended emission due to dust or gas, its point-spread function will be broader and it is that broadening we are searching for here. We compared an untrailed image of Phaethon to untrailed images of field stars from the same detector chip. The fluxes were averaged in concentric annuli centered on the centroids of the objects found using the Aperture Photometry Tool (Laher et al. 2012). Any central pixels of Phaethon at or near saturation were removed before fitting. In images where a field star appeared close to Phaethon, which included all CFHT images and six of the Gemini images, a wedge was drawn ±30° from the center of that star and was excluded before calculating the mean along each annulus. Two Gemini images with multiple background stars near Phaethon were discarded.

A Moffat function of the form shown by Equation (1) (Trujillo et al. 2001) was fit to each light profile.

$$\mathrm{PSF}(r) = A\left[1 + \left(\frac{r}{\alpha}\right)^2\right]^{-\beta}, \qquad (1)$$

where A is the amplitude, and α and β are related to the full width at half maximum (FWHM) through $\mathrm{FWHM} = 2\alpha\sqrt{2^{1/\beta} - 1}$ with $\mathrm{PSF}(\mathrm{FWHM}/2) = (1/2)\mathrm{PSF}(0)$. When fitting the profile of the star, all three parameters were allowed to vary by the fitting procedure; however, for Phaethon β was set to that found by fitting the Moffat function to the star. The light curves were then normalized to the peaks of the Moffat fits. For images where Phaethon was saturated or close to saturation by 10%, we excluded those points from the Moffat fit. This was the case for all Gemini images except for three. Sky background was subtracted by taking the mean of a few points in the tails of the distributions and subtracting from the data before the fits were made.

The Moffat fits were weighted by the uncertainties, which were assumed Poissonian and proportional to the square root of the number of photons in each annulus. The light curve of Phaethon with the Moffat stellar profile subtracted was used in order to set an upper limit on dust production. An example representing the median mass-loss rate measured is shown in Figure 1.

3.1.1. Upper Limit on Mass-loss Rate

Although the mechanisms for Phaethon's dust ejection near perihelion are not well understood, attempts have been made to calculate the mass-loss rate of Phaethon from observations to determine if it matches the total mass of the Geminid stream (see for instance, Jewitt et al. 2013; Hui & Li 2017; Ye et al. 2018). However, to date all calculations for Phaethon's dust production rate have resulted in values that are insufficient to explain the mass of the stream.

The profiles derived here for Phaethon do typically show a small excess over the profiles of nearby stars, but are all consistent within the errors with no dust production. Our primary uncertainty is in the location of the center of the PSFs. Though we use a centroiding algorithm which gives subpixel accuracy, our data points still have horizontal uncertainties of about 0.5 pixels, or ~10% of the PSF width. The fact that the residuals are highest where the PSFs are steepest and then drop off (see Figure 1) is also a hint that uncertainty is dominating the effect we see (the size of the Gemini GMOS pixels at 0″08 are relatively large, contributing to this effect). Nonetheless, from the typical excess that is seen, we can calculate an upper limit to Phaethon's mass-loss rate, dM/dt in kg s^{-1}, using Equation (2) derived from Meech et al. (1986) Equations (3)–(5), which we rewrite as:

$$\log\left(\frac{dM}{dt}\right) = \frac{30.7 - m_{\mathrm{zero}}}{2.5} - \log\left(\frac{p_v\, t\, t_{\mathrm{exp}}}{\rho\, a\, R^2\, \Delta^2\, N_e}\right), \qquad (2)$$

where m_{zero} is the zero-point magnitude specific to each detector (see Section 2), $p_v = 0.1066$ is the assumed geometric albedo of the dust grains released by Phaethon, t and t_{exp} are the diaphragm crossing time and the exposure time in seconds, $\rho = 3000$ kg m^{-3} and $a = 1\,\mu$m are the grain density and radius (Jewitt et al. 2013), R and Δ are the heliocentric and

geocentric distances in astronomical unit obtained from JPL's Horizons system (https://ssd.jpl.nasa.gov/horizons.cgi), and N_e is the number of electrons between Phaethon's and the stellar profile within the aperture.

Using Equation (2), we calculated an upper limit to Phaethon's mass-loss rate in our Gemini observations (geocentric distance $\Delta = 0.094$ au, heliocentric distance $R = 1.067$ au) at 0.2 ± 0.1 kg s^{-1}. From our CFHT observations, which were made when Phaethon was further away from the Sun ($R = 1.449$ au and $\Delta = 0.611$ au), we found the mass-loss rate to be at most 0.06 ± 0.02 kg s^{-1}. Due to their lower sensitivity, we did not use the Xingming observations for calculating the mass-loss rate.

Previous studies indicate that Phaethon shows consistent mass loss only near perihelion ($q = 0.14$ au) at a rate of 3 kg s^{-1} (Jewitt et al. 2013). Observations of Phaethon in 2003 using the 2.2 m University of Hawaii telescope, Hsieh & Jewitt (2005) put an upper limit on its mass-loss rate of ~0.01 kg s^{-1} when Phaethon was at $R = 1.60$ au and $\Delta = 1.39$ au. Our results are consistent with these, and with very low or absent dust production from Phaethon during its close approach to Earth in 2017.

3.2. Photometry: Xingming Data

The set of over 5000 raw CCD images were bias, dark, and flat-field corrected, then astrometrically calibrated with astrometry.net (Lang et al. 2010). Sources in the images were located using Source Extractor (Bertin & Arnouts 1996), and Phaethon identified from its on-sky position from an ephemeris retrieved from JPL's Horizons system.[9] A photometric calibration of each image is then performed by matching the remaining sources with stars in the UCAC4 catalog (Zacharias et al. 2013). The median numbers of star matches were 47, 65, 66, and 43 per image in the B, V, R, and I filters respectively. The UCAC4 catalog provides Johnson B and V and Sloan r' and i' magnitudes. The r' and i' magnitudes were converted to Johnson R and I magnitudes for comparison with the observations via the equations of Jordi et al. (2006). The raw images were taken in sets of five exposures of 2, 3, or 6 s per filter, and these were stacked to improve the signal-to-noise. Sixteen observations more than 0.5 mag from the daily median are rejected, as well as five anomalous points at the beginning or end of exposures sets. One two-hour set of data with a lack of suitable I-band calibrators on-image was corrected from data taken before/after; one three-hour stretch of B-filter data on December 18 with small numbers of calibrator stars on-image was omitted, leaving 1019 photometric measurements across the four filters. Colors are constructed between stacked images separated by no more than 5 minutes in time (median time between exposures used in color calculations is 1.8 minutes).

3.2.1. Colors

The mean colors of Phaethon derived from our observations are $B - V = 0.702 \pm 0.004$, $V - R = 0.309 \pm 0.003$, and $R - I = 0.266 \pm 0.004$ where the accompanying uncertainties represent the standard error of the mean. The asteroid's colors are neutral overall, slightly redder than solar in $B - V$, and slightly bluer in
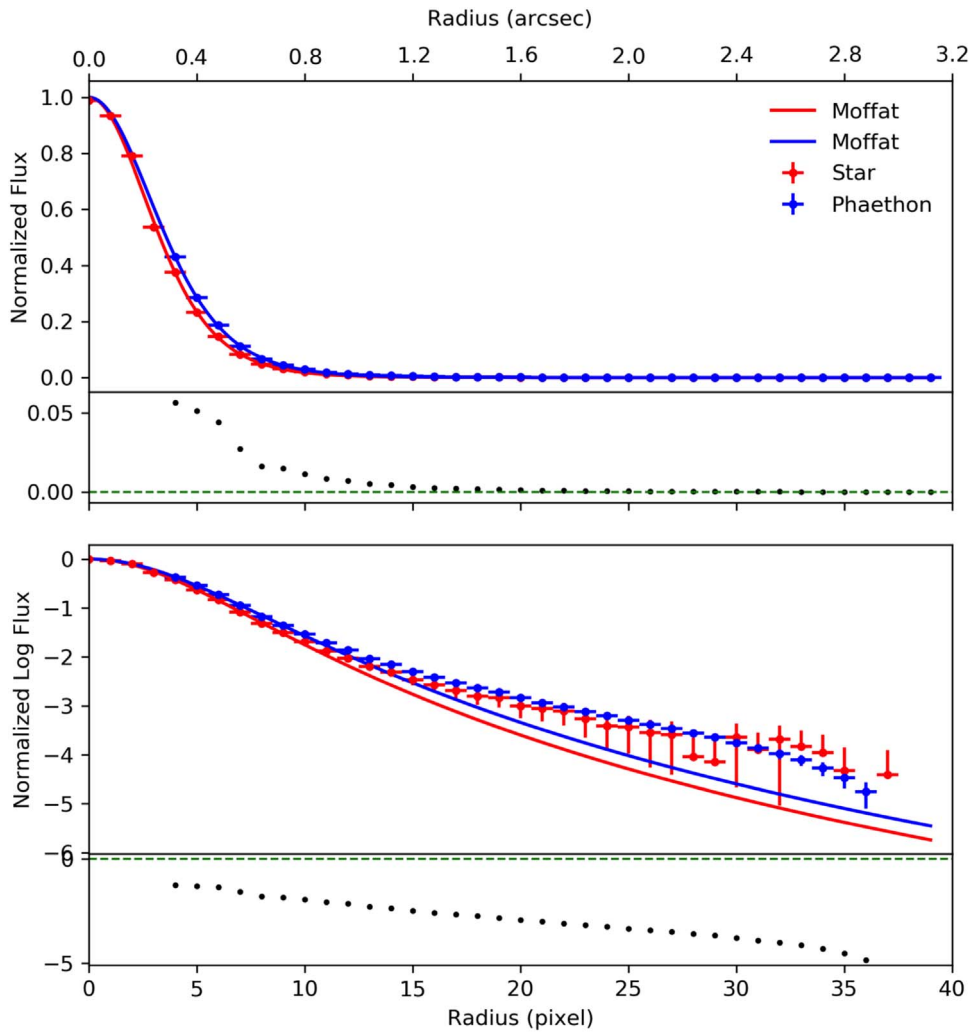
---

[9] https://ssd.jpl.nasa.gov/horizons.cgi

Figure 1. Azimuthally averaged surface brightness distribution of asteroid (3200) Phaethon from one of the Gemini images. The surface brightness distribution of a field star from the same chip is shown for comparison. The light curves have been normalized to the peaks of the Moffat fits. The Moffat fit to the star (red curve) is subtracted from Phaethon's light profile (blue points) and the residuals are shown by the black dots at the bottom of the plot. The profiles are shown in linear (top) and log (bottom) spaces. Error bars are Poissonian, proportional to the square root of the number of photons in each annulus.

$V - R$ and $R - I$, consistent with the classification of Phaethon as an F-type or B-type asteroid (Green et al. 1985; Tholen 1985).[10]

There are few published colors for Phaethon for comparison, but these are listed in Table 1. Ours are consistent with all the published values within or near the uncertainties except for our $B - V$ colors, which are redder and closer to solar colors than the other published values.

Could our redder value of $B - V$ be the result of some observational effect? The *BVRI* filters were cycled through continuously throughout the campaign, and any observations that went into a color determination were at most a few minutes apart. Late in the campaign as Phaethon moved closer to the Sun, the observations were made at larger airmasses, which might be expected to redden the colors. A reddening effect with airmass is actually excluded by our calibration of the asteroid magnitudes against catalog stars visible side-by-side with Phaethon in each image; a plot of color versus airmass is shown in Figure 2. Our method shows negligible color changes at airmasses even above 4.

---

[10] For reference, solar colors are $B - V = 0.67$, $V - R = 0.36$ and $R - I = 0.35$ (Hartmann et al. 1990; Jewitt & Luu 2001).

Table 1
Published $B - V$, $V - R$, and $R - I$ Colors of Phaethon

References	$B - V$	$V - R$	$R - I$
Skiff et al. (1996)	⋯	0.34	⋯
Dundon (2005)	0.59 ± 0.01	0.35 ± 0.01	0.32 ± 0.01
Kasuga & Jewitt (2008)	0.61 ± 0.01	0.34 ± 0.03	0.27 ± 0.04
Jewitt (2013)	0.67 ± 0.02	0.32 ± 0.02	⋯
Ansdell et al. (2014) 1997 Nov 12	0.58 ± 0.01	0.34 ± 0.01	⋯
Ansdell et al. (2014) 1997 Nov 22	0.57 ± 0.01	0.36 ± 0.01	⋯
Ansdell et al. (2014) 1995 Jan 4	0.52 ± 0.01	0.33 ± 0.01	⋯
Lee et al. (2019)	0.64 ± 0.02	0.34 ± 0.02	0.31 ± 0.03
This work	0.702 ± 0.004	0.309 ± 0.003	0.266 ± 0.004

References. Skiff et al. (1996); Dundon (2005); Kasuga & Jewitt (2008); Jewitt (2013); Ansdell et al. (2014); Lee et al. (2019).

The uncertainties quoted for our colors are the standard errors of the mean, and inherently assume that Phaethon is completely uniform in color and that the dispersion in the
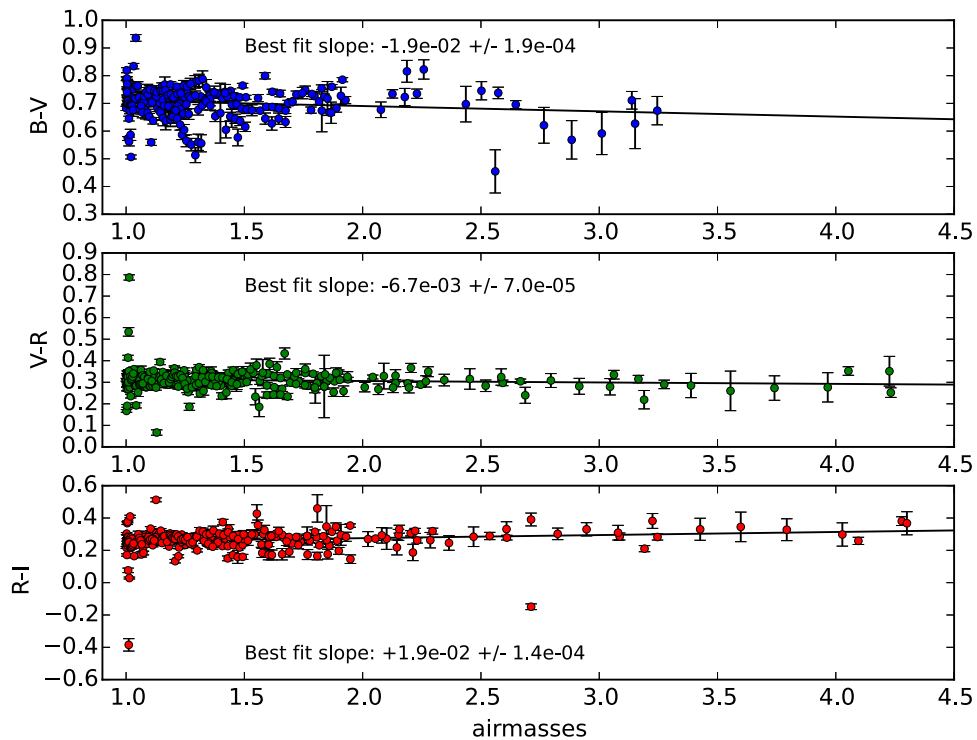
Figure 2. Phaethon's colors as a function of airmass. Best-fit slopes weighted by the photometric error are shown.
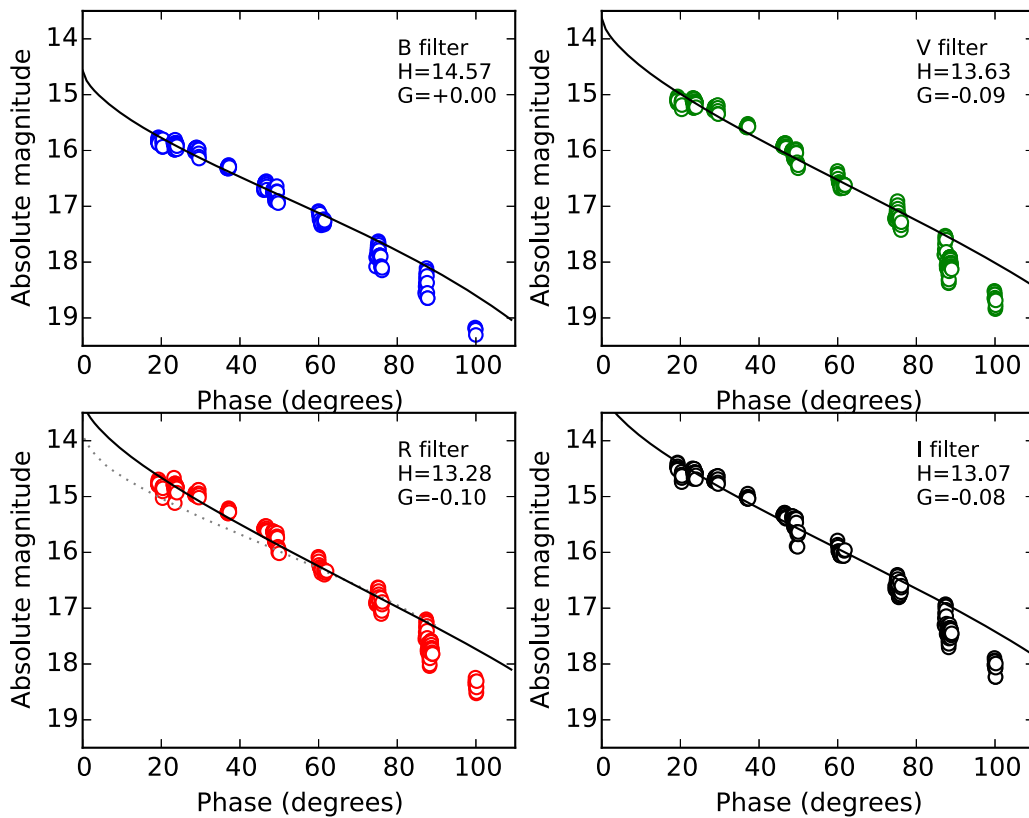

Figure 3. Phase curve of Phaethon in *BVRI* filters. A fit to the observations using the HG formalism (Bowell et al. 1989) that minimizes the residuals (weighted for photometric uncertainty) is shown with a black line. The dashed gray line in the bottom left panel shows the fit from Ansdell et al. (2014). The formal error on the observations is smaller than the plotting symbols used.

measurements is solely due to measurement error. The standard deviations of our colors are 0.06, 0.05, and 0.07 in $B-V$, $V-R$, and $R-I$, respectively, and could be indicative of real surface color variations. However it is difficult to make unambiguous statements because our observations are unresolved disk-integrated colors and Phaethon's pole solution is uncertain.

Table 2
Best-fit Values to the *H* and *G* Photometric Parameters along with Their Formal Uncertainties

Filter	H	G
B	14.57 ± 0.02	0.00 ± 0.01
V	13.63 ± 0.02	-0.09 ± 0.01
R	13.28 ± 0.02	-0.10 ± 0.01
I	13.07 ± 0.02	-0.08 ± 0.01

We are attempting to reconstruct a surface map of the albedo and/or colors of Phaethon from the photometric data and will report on this in a later paper, though this effort may not be successful unless an unambiguous pole orientation and detailed shape model becomes available.

3.2.2. Phase Curve

The phase curve of Phaethon is shown in Figure 3, covering a range of phase angles from $20°$ to over $100°$. The observations are fit using a standard HG function (Bowell et al. 1989) that minimizes the residuals (weighted by the photometric errors) using Python's scipy.optimize.curve_fit() (Jones et al. 2001); the results are in Table 2.

The *G* value in all filters is zero or slightly negative, unusual though permitted within the HG formalism of Bowell et al. (1989, see their appendix). Negative *G* values are seen in other F-type asteroids, e.g., 704 Interamnia (Lagerkvist & Magnusson 1990). Our values do differ from some recent results, e.g., Ansdell et al. (2014) who found $H = 13.90$ and $G = 0.06$ in the *R* band. However, Ansdell et al.'s (2014) observations only go up to a phase of $83°$ while ours reach $100°.2$, and large phase values tend to leverage the HG function down on its right-hand side (e.g., the lower left panel of Figure 3). Thus we believe our findings do not fundamentally conflict with those of Ansdell et al. (2014). Our data at highest phases (near $100°$) is below our fitted function, but has some of our sparsest coverage. The data covers only 60 minutes (28% of an asteroid rotation) near the minimum in the rotationally modulated light curve. The light-curve observations are presented later in Figure 7 where the highest phase observations appear in the lower panel to the far right. Thus the lower magnitude measurements at high phase are consistent with rotational modulation of the light curve due to nonsphericity of Phaethon, which is not accounted for in the HG formalism.

3.2.3. Surface Variations

The color of Phaethon as a function of observer sublatitude is shown in Figure 4. The pole solution adopted here is that of Hanuš et al. (2018), where the ecliptic longitude of the pole λ is $318°.0$, its ecliptic latitude $\beta = -47°$ and the rotation period is 3.603957 hr. We take the pole whose projection onto the celestial sphere is north of the ecliptic plane to be its north pole (with positive latitudes) according to the usual IAU definition (Archinal et al. 2011).

Figure 4 demonstrates that Phaethon's $B - V$ colors get bluer by 0.1 mag as we move from the southern hemisphere to the northern, though the $V - R$ and $R - I$ colors do not show a statistically significant similar trend. The change in $B - V$ is most apparent in Figure 4 at about $+15°$–$20°$ sublatitude. The mean value of $B - V$ south of this point is 0.71 ± 0.05, while north of it, it is 0.60 ± 0.06. Note that the Sun's sublatitude

hardly varies during our observations but remains between $-22°$ and $-24°$. As a result, the illumination of the asteroid remains nearly constant (except for its rotation) during our observations, while our vantage point moves from one that sees primarily the asteroid's southern hemisphere to one looking at its northern hemisphere over time. An animation of Phaethon's geometry relative to the Sun and Earth during the observations can be found in the animated Figure 5.

Because of the monotonic relationship between sublatitude and the phase (Sun-Target-Observer) angle in our observations, it is possible in principle that this effect is really a phase effect: the asteroid colors as a function of phase are in Figure 4 for reference. If this were the case, the asteroid would simply appear bluer in $B - V$ (but not $V - R$ or $R - I$) at large phases.

Though asteroids commonly undergo a reddening of their colors when observed at higher phases ("phase reddening"), we are not aware of any other asteroid with a trend to bluer colors with phase, and indeed B-type asteroids like Phaethon have been found not to suffer any color changes at all with phase (Lantz et al. 2018). In addition, laboratory studies have observed reddening but not blueing as a function of phase in meteoritic materials (Gradie et al. 1980; Sanchez et al. 2012); and because the phenomenon is controlled by the absorption coefficient, which is inversely proportional to the wavelength, the reflected light is expected to redden with phase on purely microphysical grounds (see Section 5 of Sanchez et al. 2012).

Our observed color variation in $B - V$ but not in other colors is consistent with the published spectral data on Phaethon. Comparisons of the asteroid's spectra show little or no variation in the red part of the optical spectrum but more pronounced variations in the *B* band (blueward of 500 nm), which corresponds with what we see in the Johnson colors (for example, Licandro et al. 2007 Figure 4 and Lazzarin et al. 2019 Figure 3 both show such comparisons).

Our observation of variations in Phaethon's colors with latitude is nominally in conflict with that of Lee et al. (2019) who concluded that Phaethon "does not have a latitudinal color variation." However, the conflict is really rather weak: their data in the northern hemisphere is limited (they reach a sublatitude only $0°.3$ north of Phaethon's equator), while we see our bluest colors only north of $+15°$. Also Lee et al. (2019) do mention a weak decrease (blueing) in spectral slope as the observer sublatitude moves north, an effect that was not statistically significant in their data but that is in accord with our findings. Lee et al. (2019) use Kim et al.'s (2018) pole solution, which is similar to the Hanuš et al. (2018) solution adopted here.

The pole of Phaethon has been determined a number of times in the last few years and the preferred solutions are clustered near the Hanuš et al. (2018) solution ($\lambda = 318°$, $\beta = -47°$) adopted here (some examples include $\lambda = 319° \pm 5$, $\beta = -39° \pm 5$ (Hanuš et al. 2016); $\lambda = 308° \pm 10$, $\beta = -52° \pm 10$ (Kim et al. 2018)). However, there are alternate poles possible, typically at similar ecliptic latitude but with the ecliptic longitude rotated by approximately $125°$, for example, $\lambda = 84° \pm 5$, $\beta = -39° \pm 5$ (Hanuš et al. 2016); $\lambda = 85° \pm 13$, $\beta = -20° \pm 10$ (Ansdell et al. 2014). The recent observations of Phaethon by Arecibo are consistent with both these possibilities (Taylor et al. 2019).

If Phaethon were found to have one of these alternate pole solutions, our observations were in fact of the northern hemisphere first, transitioning to the southern, but the basic
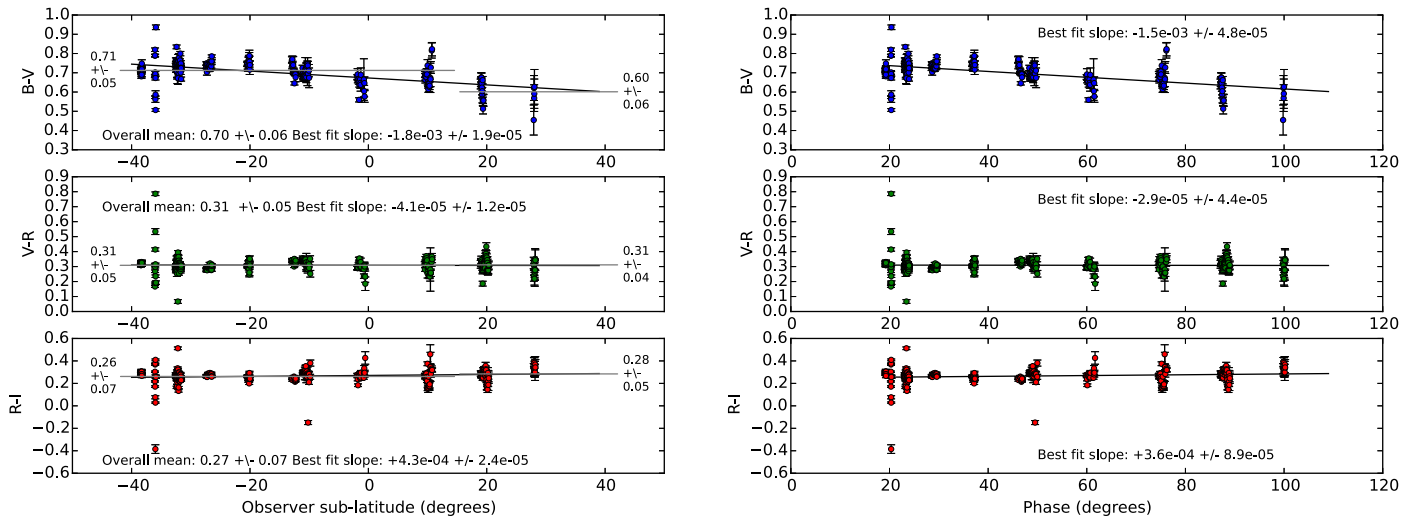
Figure 4. Left panel: Phaethon's $B - V$, $V - R$, and $R - I$ colors as a function of observer sublatitude. A linear least-squares fit is shown with a black line. The mean and one standard deviation for the values south and north of a sublatitude of $+15°$ are shown by a gray line. Right panel: Phaethon's $B - V$, $V - R$, and $R - I$ colors as a function of phase angle. A linear least-squares fit is shown with a black line.

Figure 5. Viewing geometry from Earth through the close approach of Phaethon in 2017 December. On the left is the pole solution adopted here (Hanuš et al. 2018), on the right is an alternate pole solution from Hanuš et al. (2016). Green indicates times where photometric data was taken. Ecliptic north is up.

(An animation of this figure is available.)

result is unaffected. This is because the approximate plane containing the preferred and alternate pole solutions is roughly perpendicular to our line of sight during the asteroid's close approach, and so an Earth-bound observer's sublatitude crosses Phaethon's equator at about the same time in either case (e.g., 13 hr later for the Hanuš et al. 2016 alternate pole solution). As a result, our finding of a color difference with sublatitude would still stand, but the exact distribution on the asteroid's surface would be different. A definitive pole solution is needed to settle the true spatial distribution of colors on Phaethon's surface.

Given the discussion above, we conclude that our observations reveal inherent color variations between portions of Phaethon's surface. The $B - V$ color does not, however, show a strong rotational modulation, implying large portions of the asteroid's surface are involved. Though the transition occurs as the observer moves to more northerly viewing geometries, we

continue to receive reflected light from both hemispheres. The $B - V$ change occurs as the south pole moves out of view, and so may equally be the result of a southern red region as a northern blue one. Our observations and adopted pole solution point to latitudinal color differences on Phaethon's surface but, because we are seeing unresolved disk-integrated colors, and Phaethon's pole solution is uncertain, and we see other color variations occurring on shorter timescales, we cannot conclude that Phaethon's color variations are associated purely with its rotational hemispheres. Nonetheless substantial large-scale color variations are strongly implied by our observations.

A latitude-dependent color difference on Phaethon could be due to differences in solar heating. Ohtsuka et al. (2009) and Ansdell et al. (2014) found that the northern latitudes of Phaethon would be preferentially heated and bluer in $B - V$, using the pole solution of Krugly et al. (2002). However, Hanuš et al. (2016) argued, using an updated pole solution, that
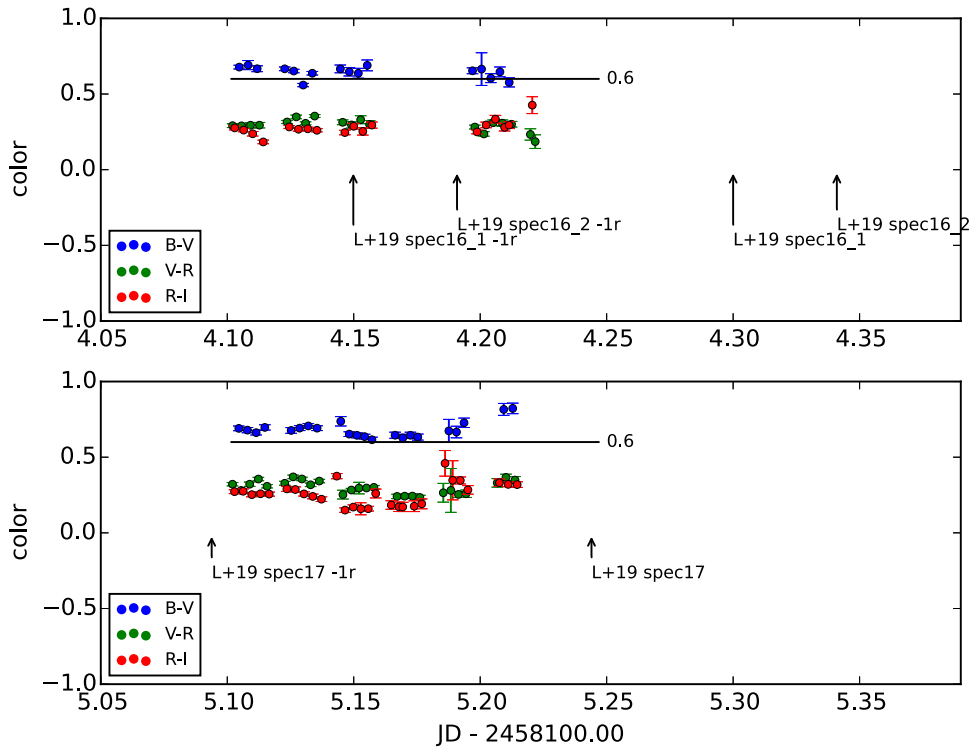
Figure 6. Phaethon's $B - V$, $V - R$, and $R - I$ colors near the time of Lazzarin et al.'s (2019) observations (two spectra taken December 16: spec16_1 and spec16_2, and 1 spectrum on December 17:spec17). Integer numbers of rotations from their observations are indicated by black arrows, e.g., +1r means one rotation later. Our observations that correspond most closely in time with theirs are indicated by the red arrow. We see a reddening of the colors especially in $B - V$ just before their spec17 is taken, which is consistent with their results.

Phaethon has not suffered preferential heating over the last thousands of years.

Comparisons of our results with these previously published ones are complicated by nonstandard definitions of north. Ohtsuka et al. (2009) "define Phaethons north-pole orientation as the sunlit side at the perihelion" and Ansdell et al. (2014) seem to follow this choice. This puts both of their chosen "north" poles south of the invariable plane, in contravention of current IAU guidelines (Archinal et al. 2011). However, if we compute the observer sublatitudes using their (Krugly et al. 2002) pole solution and assume this flip of definitions, then our results qualitatively agree with Ohtsuka et al. (2009) and Ansdell et al. (2014) that there is a trend with observer sublatitude on Phaethon.

The color difference almost certainly stems from compositional variations across the surface. Determining whether solar heating is a possible cause will likely require a definitive pole solution but in the absence of preferential heating, the excavation of fresh material by cratering events seems a likely cause. Radar observations from Arecibo (Taylor et al. 2019) indicate what could be kilometer-sized craters at latitudes of $+10°$ and $+20°$ north ("Candidate Concavities" b and c in their Table 2, also discussed in Section 3.2.4 below). The production of these craters could have both spread fresh as-yet-unspaceweathered material across the asteroid's surface, while releasing a large amount of material into the Geminid meteoroid stream without the need for traditional cometary activity.

The Geminid meteoroid stream mass is very uncertain, and has been estimated to contain from 10^{14} g (Beech 2002) to over 10^{16} g of material (Hughes & McBride 1989; Blaauw 2017), with some calculations reaching 10^{18} g (Ryabova 2017). The

excavation of a kilometer-class crater on Phaethon might release $\sim 10^{15}$ g of material, so the Geminid meteoroid stream could plausibly be populated by a single or perhaps a few large impacts on its surface, if the lower estimates of the stream mass are correct. The current rate of loss of material from Phaethon's surface due to meteoroid impacts (1 ton per year; Szalay et al. 2019) is too small to account for the Geminid stream.

3.2.4. Comparison with Other Observations

Lazzarin et al. (2019) report on optical spectra during the close approach, and find a reddening of Phaethon blueward of 500 nm (in the B band) from December 16 to 17. Our observations do not precisely overlap in time with those of Lazzarin et al. (2019) but we see something consistent with their reports. Our colors become redder near the end of our observations on December 17, just before Lazzarin et al. (2019) begin to observe on December 17 (see Figure 6). Our observations finish less than an hour before their spectra are taken, corresponding to about a quarter rotation of the asteroid.

Radar observations of Phaethon by Arecibo (Taylor et al. 2019) in 2017 indicate surface features (concavities, boulders) that might be correlated with features in the asteroid's light curve or colors. Because the Xingming observatory is on the other side of the globe from Arecibo, our observations are not coincident with theirs. However, we can compare our observations at integer numbers of the asteroid's rotation period, which we here assume is 3.603957 hr (Hanuš et al. 2018; Kim et al. 2018). Figure 7 shows our light curve in the $BVRI$ filters during our observations closest in time to the Arecibo observations. The radar-observed features (which Taylor et al. 2019 label a through e in their Table 2) are not associated with any obvious changes in the light curve, with the
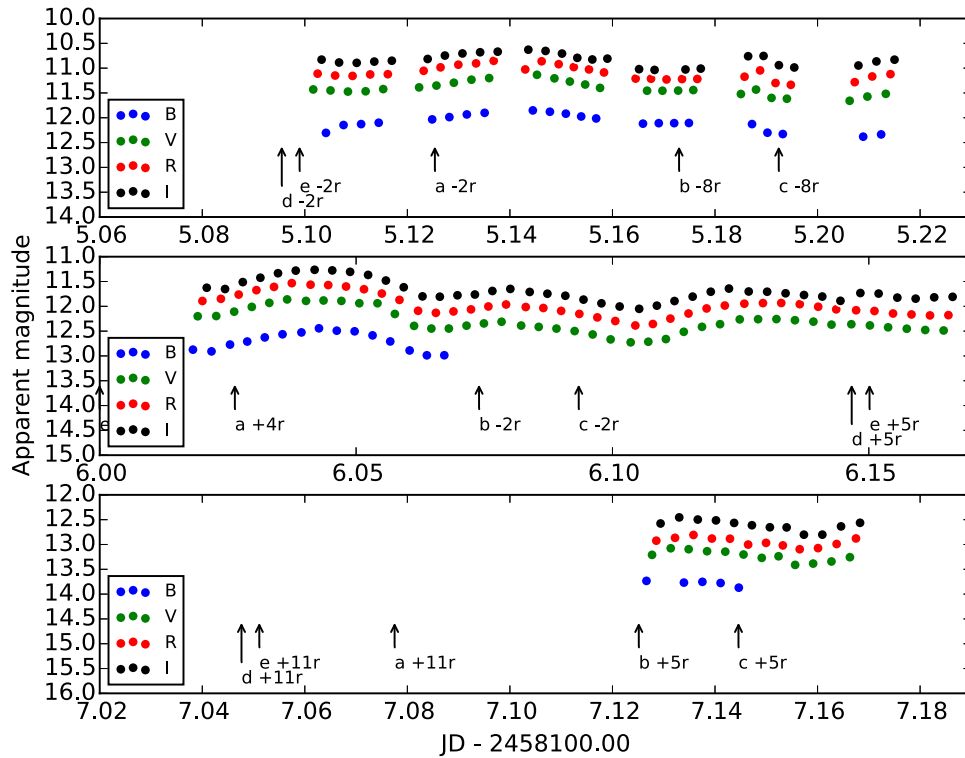
Figure 7. Light curve of Phaethon nearest the features reported by Taylor et al. (2019). Features are (a) Candidate Boulder, (b) Candidate Concavity, (c) Candidate Concavity, (d) Linear Facet, and (e) Polar Dark Spot. Arrows indicate integer numbers of rotations from the reported subobserver time, e.g., +1r means one rotation later. The formal error bars on the measurements are smaller than the plotting symbols.

exception of b and c, both termed "candidate concavities" by Taylor et al. (2019). Both of these occur near broad dips in the light curves in all filters on all three days. Though light-curve variations could be accounted for by the nonsphericity of the asteroid, we note that Phaethon's rotation would have carried features at the latitudes of Taylor et al.'s (2019) candidate concavities b and c from the far side of the asteroid across the illuminated limb and then across the terminator during this time. The terminator was roughly line with the Earth on the dates of observation (see animated Figure 5), and so any features would have been in sunlight for approximately one hour (0.04 days) on these dates, corresponding to the duration of the dips seen in the light curve. This would provide plenty of opportunity for shadowing effects from obliquely illuminated concavities to create brightness variations. The light-curve variations seen in Figure 7 have this timescale, and thus are at least in principle consistent with craters on Phaethon.

Also, returning to the discussion of the phase curves in Section 3.2.2, we note that candidate concavities b and c are near the subobserver point at the rightmost edge of the lower panel, when our last photometric data were taken and corresponding to our highest phase angles ($\sim$100°). These features correspond with a relatively dimmer portion of the rotationally modulated light curve (compare, for example, with the middle panel of Figure 7). Thus the relative lowness of our data with respect to the fit at high phase angles in Figure 3 is simply the result of rotational undersampling the light curve at these difficult-to-observe phases.

3.3. Fragmentation: CFHT Data

Given an absence of cometary activity for Phaethon, other mass loss or fragmentation processes must be invoked to

explain the Geminid meteor stream. To examine the possibility that Phaethon has undergone coarse fragmentation through collision or other processes, a search for fragments near Phaethon with the *Hubble Space Telescope* was performed as part of this campaign, but no fragments were seen: these result were reported earlier in Ye et al. (2018). Jewitt et al. (2018) performed *HST* observations of Phaethon near the same time, also without seeing any fragments.

In addition, four CFHT Megacam images (*g* filter) obtained on 2017 November 15 12:30:22.74 UT–13:24:43.16 UT with 900 s exposure times were searched for objects with on-sky motion close to Phaethon's. Tracking at Phaethon's on-sky speed provides improved sensitivity to objects moving along on similar trajectories.

The premise being examined here is that if Phaethon has fragmented in the past, it might still be accompanied by daughter asteroids that are traveling in nearly the same orbit. Such fragments will disperse away from Phaethon over time but if Phaethon underwent such fragmentation recently, then pieces could still be near it.

While at closest approach, Phaethon would have been at an ecliptic latitude of 22° in Andromeda, traveling at a rate of over 2000″ per hour, making it and any comoving fragments easy to distinguish from background asteroids. Unfortunately, the geometry at which the images were taken was somewhat before the closest approach owing to the vagaries of the telescope's queue observing system. The images were taken a few weeks early and at that time, Phaethon was at an ecliptic latitude of 13° in the constellation Auriga moving at 20″38 hr^{-1}, −5″78 hr^{-1} in R.A.cos(decl.), and 19″55 hr^{-1} in decl. on the sky. Five fragment candidates were identified moving at speeds between 15 and 25 arcsec hr^{-1} and with on-sky directions of motion within 5° of Phaethon's during the
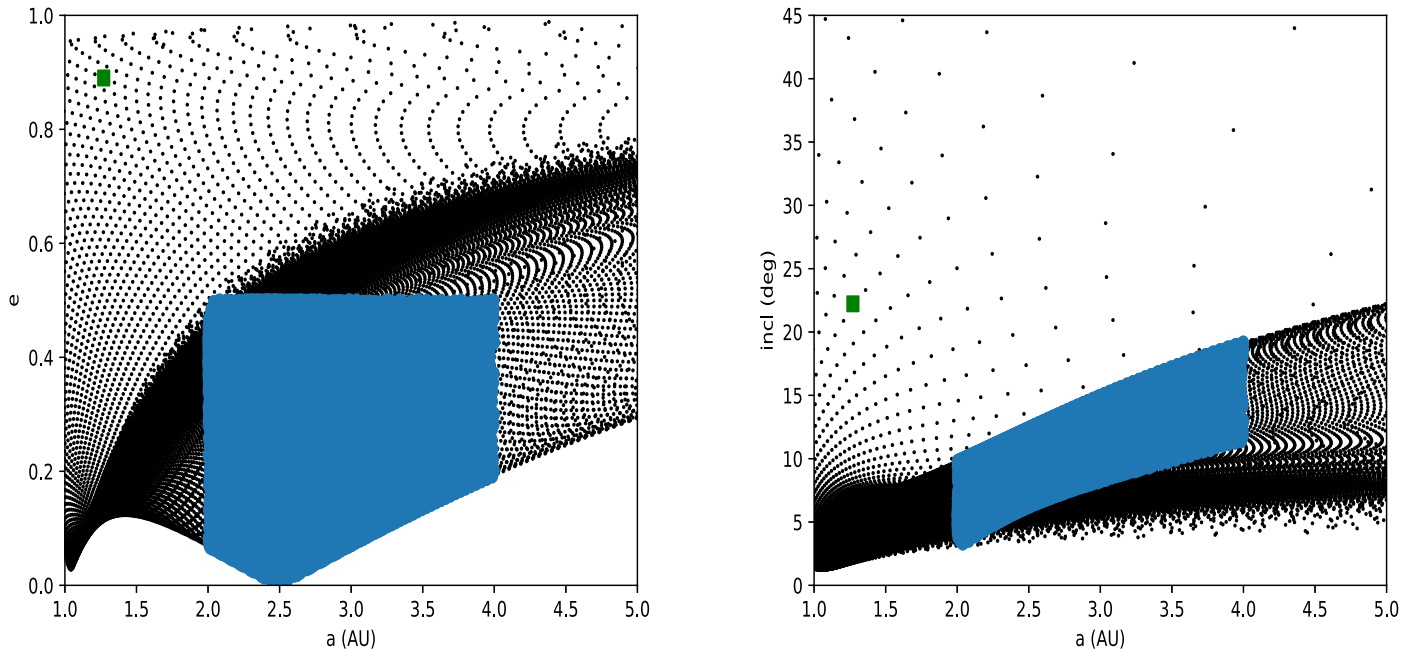
Figure 8. Black dots indicate orbital elements that would have on-sky motions observable from CFHT on 2017 November 15 13:00 UT consistent with that observed for Phaethon. Phaethon's values are indicated by the green square. Blue dots indicate values consistent in all three of a, e, and i with the asteroid belt (see the text for details).

0.91 hr arc of the images. All were fainter than apparent g magnitude 22.5 (Phaethon was at $m_g = 16$ at the time), and none were identified as known main-belt asteroids by the Minor Planet Center's MPChecker.[11]

Though the candidate fragments have the on-sky coordinates and rates of motion similar to Phaethon's, it is possible for background or foreground asteroids to do the same but without being on the same orbit as Phaethon. Such objects would have on-sky motions similar to Phaethon's but would not be related to it. We can show that unfortunately, because of the suboptimal time at which our observations were taken, main-belt asteroids could display rates of motion similar to Phaethon's. Figure 8 displays the semimajor axis a, eccentricity e, and inclination i values that could have produced on-sky motions similar to Phaethon's. The blue region indicates orbital element sets that simultaneously satisfy all three of $2 < a < 4$ au, $e < 0.5$, and $i < 45°$, and thus could plausibly be produced by main-belt asteroids. Given the abundance of main-belt orbits that could mimic the on-sky motion of Phaethon, we cannot conclude that our candidates are fragments. However, we list them here (and have reported them to the Minor Planet Center) for completeness (see Table 3), in the hope that a link or absence thereof to Phaethon can be clarified in the future.

4. Summary and Conclusions

Ground-based observations of asteroid 3200 Phaethon were made in 2017 December. Phaethon's colors and phase curve were measured, and the asteroid was examined for possible cometary activity and fragmentation. Our results are consistent with previous findings of neutral to blue colors overall, though we find a redder $B - V$ color than previous studies. The phase curve of Phaethon is extended to over $100°$ in the $BVRI$ filters. Large-scale changes in the $B - V$ colors of Phaethon were observed that are not easily dismissed as phase or airmass

Table 3
Candidate Fragment Information, Including Time of Observation, R.A., Decl., and Apparent Magnitude in the g Filter

Fragment #	Date of Observation	R.A.	Decl.	Mag
1	2017 11 15.52631	07 07 33.98	+36 04 58.9	22.8
	2017 11 15.53720	07 07 33.89	+36 05 02.7	22.9
	2017 11 15.55315	07 07 33.76	+36 05 08.3	22.9
	2017 11 15.56404	07 07 33.67	+36 05 12.2	22.6
2	2017 11 15.52631	07 07 02.07	+36 10 40.4	22.9
	2017 11 15.53720	07 07 01.97	+36 10 44.2	22.7
	2017 11 15.55315	07 07 01.80	+36 10 50.0	22.7
	2017 11 15.56404	07 07 01.69	+36 10 53.9	22.5
3	2017 11 15.52631	07 07 32.02	+35 47 28.5	24.3
	2017 11 15.53720	07 07 31.90	+35 47 33.8	24.6
	2017 11 15.55315	07 07 31.76	+35 47 42.1	23.1
	2017 11 15.56404	07 07 31.63	+35 47 46.8	24.4
4	2017 11 15.52631	07 05 30.17	+35 43 10.2	24.7
	2017 11 15.53720	07 05 30.07	+35 43 15.7	24.7
	2017 11 15.56404	07 05 29.84	+35 43 29.2	24.6
5	2017 11 15.53720	07 08 03.36	+35 34 42.8	23.9
	2017 11 15.55315	07 08 03.23	+35 34 48.9	23.9
	2017 11 15.56404	07 08 03.14	+35 34 53.3	24.3

effects, while the $V - R$ and $R - I$ colors remain constant. Variations in the light curve consistent with craters reported by Taylor et al. (2019) were seen: craters that could be the source of the Geminid meteoroid stream material. There was an absence of cometary activity down to an upper limit on the mass production rate of $0.06 \pm 0.02 \, \text{kg s}^{-1}$ when the asteroid was at a heliocentric distance of 1.449 au, and $0.2 \pm 0.1 \, \text{kg s}^{-1}$ when at a heliocentric distance of 1.067 au. No fragments were found that could unequivocally be linked to Phaethon.

---

[11] https://www.minorplanetcenter.net/cgi-bin/checkmp.cgi

ORCID iDs

Maryam Tabeshian ⬥ https://orcid.org/0000-0003-1841-5442
Paul Wiegert ⬥ https://orcid.org/0000-0002-1914-5352
Quanzhi Ye ⬥ https://orcid.org/0000-0002-4838-7676
Man-To Hui ⬥ https://orcid.org/0000-0001-9067-7477

References

Ansdell, M., Meech, K. J., Hainaut, O., et al. 2014, ApJ, 793, 50
Archinal, B. A., A'Hearn, M. F., Bowell, E., et al. 2011, CeMDA, 109, 101
Beech, M. 2002, MNRAS, 336, 559
Bertin, E., & Arnouts, S. 1996, A&AS, 117, 393
Blaauw, R. C. 2017, P&SS, 143, 83
Boice, D. C., Benkhoff, J., & Huebner, W. F. 2013, BAAS, 45, 413.32
Boulade, O., Charlot, X., Abbon, P., et al. 2003, Proc. SPIE, 4841, 72
Bowell, E., Hapke, B., Domingue, D., et al. 1989, in Asteroids II, ed. R. Binzel, T. Gehrels, & M. Matthews (Tucson, AZ: Univ. Arizona Press), 524
Davies, J. K. 1986, MNRAS, 221, 19P
de León, J., Campins, H., Tsiganis, K., Morbidelli, A., & Licandro, J. 2010, A&A, 513, A26
Delsemme, A. H., & Miller, D. C. 1971, P&SS, 19, 1229
Dundon, L. 2005, M.s. thesis, U. Hawaii
Gradie, J., Veverka, J., & Buratti, B. 1980, LPSC, 11, 799
Green, S. F., Meadows, A. J., & Davies, J. K. 1985, MNRAS, 214, 29P
Hanuš, J., Delbo, M., Vokrouhlický, D., et al. 2016, A&A, 592, A34
Hanuš, J., Vokrouhlický, D., Delbo, M., et al. 2018, A&A, 620, L8
Hartmann, W. K., Tholen, D. J., Meech, K. J., & Cruikshank, D. P. 1990, Icar, 83, 1
Hsieh, H. H., & Jewitt, D. 2005, ApJ, 624, 1093
Hughes, D. W., & McBride, N. 1989, MNRAS, 240, 73
Hui, M.-T., & Li, J. 2017, AJ, 153, 23
Jewitt, D. 2013, AJ, 145, 133
Jewitt, D., & Li, J. 2010, AJ, 140, 1519
Jewitt, D., Li, J., & Agarwal, J. 2013, ApJL, 771, L36
Jewitt, D., Mutchler, M., Agarwal, J., & Li, J. 2018, AJ, 156, 238
Jewitt, D. C., & Luu, J. X. 2001, AJ, 122, 2099
Jones, E., Oliphant, T., Peterson, P., et al. 2001, SciPy: Open Source Scientific Tools for Python, http://www.scipy.org/
Jordi, K., Grebel, E. K., & Ammon, K. 2006, A&A, 460, 339
Kasuga, T., & Jewitt, D. 2008, AJ, 136, 881
Kim, M.-J., Lee, H.-J., Lee, S.-M., et al. 2018, A&A, 619, A123
Krugly, Y. N., Belskaya, I. N., Shevchenko, V. G., et al. 2002, Icar, 158, 294
Lagerkvist, C.-I., & Magnusson, P. 1990, A&AS, 86, 119
Laher, R. R., Gorjian, V., Rebull, L. M., et al. 2012, PASP, 124, 737
Lang, D., Hogg, D. W., Mierle, K., Blanton, M., & Roweis, S. 2010, AJ, 137, 1782
Lantz, C., Binzel, R. P., & DeMeo, F. E. 2018, Icar, 302, 10
Lazzarin, M., Petropoulou, V., Bertini, I., et al. 2019, P&SS, 165, 115
Lee, H.-J., Kim, M.-J., Kim, D.-H., et al. 2019, P&SS, 165, 296
Li, J., & Jewitt, D. 2013, AJ, 145, 154
Licandro, J., Campins, H., Mothé-Diniz, T., Pinilla-Alonso, N., & de León, J. 2007, A&A, 461, 751
Meech, K. J., Jewitt, D., & Ricker, G. R. 1986, Icar, 66, 561
Ohtsuka, K., Nakato, A., Nakamura, T., et al. 2009, PASJ, 61, 1375
Ryabova, G. O. 2007, MNRAS, 375, 1371
Ryabova, G. O. 2017, P&SS, 143, 125
Sanchez, J. A., Reddy, V., Nathues, A., et al. 2012, Icar, 220, 36
Skiff, B. A., Buie, M. W., & Bowell, E. 1996, BAAS, 28, 1104
Szalay, J. R., Pokorný, P., Horányi, M., et al. 2019, P&SS, 165, 194
Taylor, P. A., Rivera-Valentin, E. G., Benner, L. A. M., et al. 2019, P&SS, 167, 1
Tholen, D. J. 1985, IAUC, 4034
Trujillo, I., Aguerri, J. A. L., Cepa, J., & Gutiérrez, C. M. 2001, MNRAS, 328, 977
Whipple, F. L. 1983, IAUC, 3881
Ye, Q., Wiegert, P. A., & Hui, M.-T. 2018, ApJL, 864, L9
Yu, L., Ip, W.-H., & Spohn, T. 2019, MNRAS, 482, 4243
Zacharias, N., Finch, C. T., Girard, T. M., et al. 2013, AJ, 145, 44